JOC The Journal of Organic Chemistry

Article

pubs.acs.org/joc

Origin of Inversion versus Retention in the Oxidative Addition of 3-Chloro-cyclopentene to Pd(0)L_n

Larry M. Wolf and Walter Thiel*

Max-Planck-Institut für Kohlenforschung, Kaiser-Wilhelm-Platz 1, 45470 Mülheim an der Ruhr, Germany

Supporting Information

ABSTRACT: The preference for *syn* versus *anti* oxidative addition of 3-chloro-cyclopentene to Pd(0)L_n was investigated using density functional theory (L = PH_3, PMe_3, PF_3, ethylene, maleic anhydride, pyridine, imidazol-2-ylidene). Both mono- and bis-ligation modes were studied (n = 1 and 2). The pathways were analyzed at the B2PLYP-D3/def2-TZVPP//TPSS-D3/def2-TZVP level, and an interaction/distortion analysis was performed at the ZORA-TPSS-D3/TZ2P level for elucidating the origin of the selectivity preferences. Mechanistically, the *anti* addition follows an S_N2 type mechanism, whereas the *syn* addition has partial S_N1 and S_N2' character. Contrary to the traditional rationale that orbital interactions are dominant in the *anti* pathway, analysis of the variation of the interaction components along the intrinsic reaction coordinate shows that the *syn* pathway exhibits stronger overall orbital interactions. This orbital preference for the *syn* pathway diminishes with increasing donor capacity of the ligand. It is caused by the donation of the isolated p orbitals on the migrating chlorine atom to the PdL_n fragment, which is lacking in the *anti* pathway, whereas the HOMO−LUMO overlap between the fragments is greater for the *anti* pathway. Electrostatically, the *syn* pathway is preferred for weakly donating and withdrawing ligands, whereas the *anti* pathway is favored with strongly donating ligands.

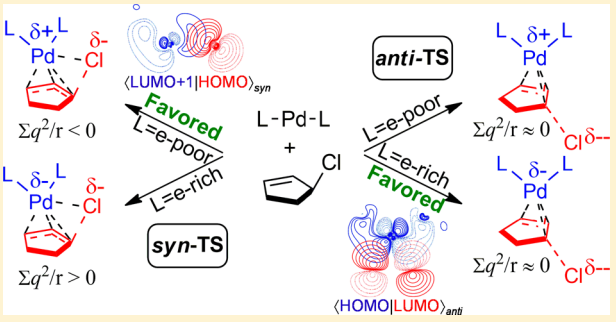

INTRODUCTION

One of the preeminent synthetic methods for the stereoselective construction of carbon−carbon bonds is palladium-catalyzed allylic alkylation.[1] The wide use of this transformation can largely be attributed to the high predictability of the stereochemical course of the reaction. The reliability and ubiquity of this transformation has called for insight from computation, principally density functional theory (DFT).[2]

The selectivity in the overall transformation is thought to be controlled both by the oxidative addition step and the mode by which the incoming nucleophile adds to the complex. The addition normally occurs via attack at the palladium or at one of the termini of the allyl moiety. In rare cases, the central carbon can undergo electrophilic attack, resulting in the formation of cyclopropanes.[3] The general reactivity of palladium allylic moieties has been investigated extensively computationally. The reactivity and selectivity is highly dependent on the reaction conditions including the choice of nucleophile,[4] ligand,[5] solvent,[4a] and the presence of other additives.

While the oxidative addition step, depending on overall energetics, may influence the selectivity to a similar extent as the nucleophilic addition step, it has received less scrutiny. Oxidative addition of alkyl and aryl systems has received more attention,[5c,6] for which the fundamentals are well-established. Oxidative addition is commonly accepted to proceed through inversion of configuration at the substituting center for sp^3-hybridized alkyl and allylic systems (Scheme 1). The *syn* selective oxidative addition, in which the transition metal adds to the same face as the leaving group, has been demonstrated to depend on the solvent medium and the chosen ligands. Electron-deficient ligands combined with nonpolar solvents lead to *syn* selective oxidative addition, whereas the use of electron-donating ligands combined with polar solvents tends to result in PdL_n adding in an *anti* fashion (i.e., the transition metal adds to the face opposite the leaving group).[7]

Despite numerous investigations into palladium-catalyzed allylic alkylation, the factors controlling the selectivity in the

Scheme 1

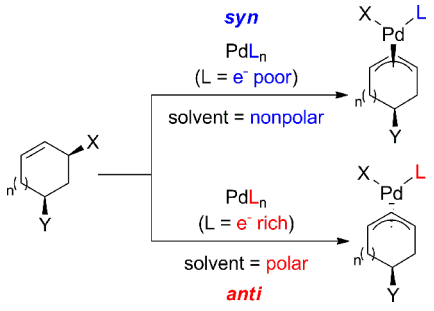

Special Issue: Mechanisms in Metal-Based Organic Chemistry

Received: August 31, 2014
Published: September 30, 2014

   dx.doi.org/10.1021/jo5020068 | J. Org. Chem. 2014, 79, 12136−12147

oxidative addition step are not yet well established. The aim of the present computational study is to garner additional conceptual insight into the oxidative addition step by elucidating the origin of the intrinsic preference for *syn* or *anti* addition and the influence of ligands and solvation on this preference.

COMPUTATIONAL METHODS

Geometry optimizations were performed with Gaussian09[8] program package. All geometries were fully optimized without symmetry constraints using the TPSS functional[9] and the def2-TZVP[10] basis set for all atoms, augmented by the D3 dispersion correction with BJ-damping[11] (TPSS-D3). The 28 inner-shell core electrons of the palladium atom were described by an effective core potential[12] accounting for scalar relativistic effects (def2-ecp). An auxiliary basis was used for density fitting of the Coulomb potentials.[13] Stationary points were characterized by evaluating the harmonic vibrational frequencies at the optimized geometries. Zero-point vibrational energies (ZPVE) were computed from the corresponding harmonic vibrational frequencies without scaling. The thermal and entropic contributions were evaluated within the rigid-rotor harmonic-oscillator approximation. Free energies were determined at standard pressure (1 bar) and at room temperature (298.15 K). The nature of all transition states was verified by following the intrinsic reaction coordinates.[14] Single-point calculations were performed with the B2PLYP[15] double hybrid functional employing the def2-TZVPP[10] basis set both in the gas phase and in solution using the conductor-like polarizable continuum model (CPCM)[16] with benzene as solvent (with UAKS radii for all atoms). Partial charges were determined using the natural bond order (NBO) analysis[17] and the Voronoi deformation density approach (VDD).[18]

Energy decomposition analysis (EDA) was performed on the TPSS-D3/def2-TZVP optimized geometries using the ADF2013[19] program package at the TPSS level in conjunction with a triple-ζ-quality basis set using uncontracted Slater-type orbitals (STOs)[20] augmented with two sets of polarization functions for all atoms; all electrons were included (i.e., inner core electrons were not described by a frozen core). Scalar relativistic effects were accounted for using the zeroth-order regular approximation (ZORA).[21] This level is denoted TPSS-D3/TZ2P//TPSS-D3/def2-TZVP.

An EDA provides qualitative insight into the physical origin of bonding interactions. In the scheme developed independently by Morokuma[22a] and Ziegler and Rauk,[22b,c] the bonding energy between the bonded fragments is divided into the distortion energy ΔE_{dist}, the energy required to distort the nuclei of the fragment equilibrium geometries into the geometries in the corresponding complex, and the interaction energy ΔE_{int}, the energy released upon allowing the distorted fragments to interact to form the complex.

$$\Delta E = \Delta E_{dist} + \Delta E_{int} \quad (1)$$

The interaction energy ΔE_{int} is further decomposed into components that can provide insight into the nature of the bonding interactions

$$\Delta E_{int} = \Delta E_{elstat} + \Delta E_{Pauli} + \Delta E_{orb} + \Delta E_{disp} \quad (2)$$

where ΔE_{elstat} is the classical electrostatic interaction energy between the unperturbed charge distributions of the distorted fragments. The Pauli repulsion term ΔE_{Pauli} accounts for the repulsion between occupied orbitals of the fragments originating from the inability of electrons with the same spin to occupy the same region of space; it arises from antisymmetrization of the product of the unperturbed fragment wave functions. The orbital interaction term ΔE_{orb} comprises interfragment charge transfer (mixing of occupied orbitals of one fragment with unoccupied orbitals of the other fragment and vice versa) as well as the intrafragment charge transfer (mixing of empty and occupied orbitals within each fragment), which result from allowing the orbitals to fully relax after the antisymmetrization step. The dispersion term ΔE_{disp} is computed from the DFT-D3 empirical correction.

These terms were also analyzed along the reaction coordinate to gain insight into the origin of the reaction barriers through an adapted interaction/distortion or strain analysis.[23] The transition state corresponds to a maximum along the reaction coordinate, at which the following relationship holds

$$\frac{d\Delta E_{int}}{d\Delta E_{dist}} = \frac{d(\Delta E_{elstat} + \Delta E_{Pauli} + \Delta E_{orb} + \Delta E_{disp})}{d\Delta E_{dist}} = -1 \quad (3)$$

Equation 3 indicates that the transition state is reached when a small increase in the distortion energy gives rise to an equivalent gain in the overall interaction energy. Hence, analyzing the components of the interaction energy as a function of the distortion energy furnishes direct insight into the factors governing the location of the transition state, through graphical analysis of the distortion profiles of the interaction energy components. Therefore, the EDA will be performed both along an energy distortion coordinate and a geometrically defined reaction coordinate.

RESULTS AND DISCUSSION

As model substrate, we chose 3-chloro-cyclopentene, which represents a compromise between comparatively strain-free cyclohexene substrates and strained cyclobutene substrates that have recently been introduced to allylic substitution.[24] Experimentally, chloro-cyclopentene substrates afford results similar to chloro-cyclohexene substrates.[25] To assess how the electronic structure of the ligand influences the selectivity preference, we explored several ligands of variable electron-donating and -withdrawing capacity. Phosphines (**PMe_3**, **PH_3**), pyridine (**Pyr**), and a model N-heterocyclic carbene (**NHC**) were harnessed for their donating ability, whereas various π-acids (**PF_3**, **MA**, and **Et**) were explored for their withdrawing capacity (Figure 1).

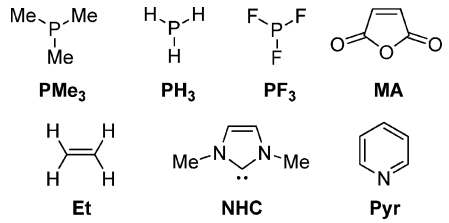

Figure 1. Ligands explored in the present computational mechanistic investigations.

The *anti* and *syn* mechanisms could proceed via pathways with one or two ligands bound (Table 1). The bis-ligated pathway is often proposed, although ligand dissociation may be preferred for strongly electron-withdrawing ligands. Mono-ligated palladium has been demonstrated computationally to be preferred in the oxidative addition of aryl iodides in some cases.[26] Oxidative addition through the *syn* pathway takes place by a direct insertion mechanism to generate an intermediate that may exist in equilibrium with the ligand dissociated.

The mechanism was computed at the B2PLYP-D3/def2-TZVPP//TPSS-D3/def2-TZVP level. The TPSS functional produces good geometries for transition metals[27] including palladium complexes.[28] The B2PLYP functional has been demonstrated to afford good barrier heights in palladium chemistry and organometallic chemistry in general.[28,29] The reaction barriers afforded by the TPSS-D3/def2-TZVP energies are ~2−4 kcal/mol lower than those from B2PLYP, which is typical for nonhybrid functionals. Nevertheless, the two functionals give the same trends in the energies.[30] Ligand

dx.doi.org/10.1021/jo5020068 | J. Org. Chem. 2014, 79, 12136−12147

Table 1. Investigated Pathway with the Corresponding Free Energies ΔG (kcal/mol) Computed at the B2PLYP-D3/def2-TZVPP//TPSS-D3/def2-TZVP Level[a]

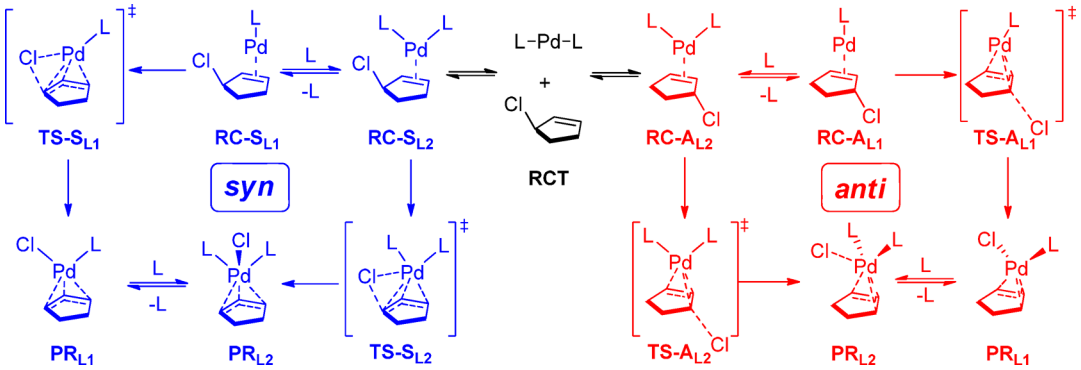

	RCT	RC-A$_{L2}$	RC-S$_{L2}$	TS-A$_{L2}$	TS-S$_{L2}$	PR$_{L2}$
MA	0.0[0.0]	−16.3[−11.8]	−16.2[−11.2]	28.6[23.6]	4.2[8.5]	–
Et	0.0[0.0]	−8.2[−7.8]	−5.9[−5.2]	25.7[13.3]	16.4[13.8]	0.4[−3.1]
PF3	0.0[0.0]	−12.6[−10.8]	−11.1[−9.2]	27.4[15.3]	10.5[9.7]	−4.8[−5.7]
PH3	0.0[0.0]	−7.7[−8.2]	−6.4[−6.4]	20.1[5.1]	11.1[7.3]	−6.6[−10.5]
PMe3	0.0[0.0]	−11.2[−11.0]	−9.0[−7.8]	8.3[−4.7]	1.3[−0.4]	−19.6[−22.1]
Pyr	0.0[0.0]	−12.0[−12.1]	−11.4[−10.5]	5.4[−8.2]	0.4[−0.3]	−23.4[−25.4]
NHC	0.0[0.0]	−6.1[−5.4]	−5.2[−3.4]	6.1[−5.2]	5.4[5.4]	−15.4[−17.6]
	RCT	**INT-A$_{L1}$**	**INT-S$_{L1}$**	**TS-A$_{L1}$**	**TS-S$_{L1}$**	**PR$_{L1}$**
MA	0.0[0.0]	−3.6[−1.5]	−4.7[−1.5]	40.9[31.2]	2.7[4.9]	−12.9[−11.7]
Et	0.0[0.0]	−0.3[−0.3]	0.7[0.6]	36.3[21.2]	10.7[9.5]	−11.0[−14.7]
PF3	0.0[0.0]	3.7[4.5]	3.8[4.6]	45.1[30.1]	14.0[13.7]	−10.0[−9.5]
PH3	0.0[0.0]	4.9[4.0]	5.7[4.6]	37.9[21.7]	16.9[14.6]	−10.0[−14.3]
PMe3	0.0[0.0]	9.7[9.7]	11.2[11.0]	35.2[22.3]	20.9[19.6]	−11.7[−14.6]
Pyr	0.0[0.0]	−9.6[−9.9]	−8.1[−8.0]	18.2[4.9]	5.8[4.6]	−27.7[−30.9]
NHC	0.0[0.0]	11.9[11.5]	12.8[12.7]	38.7[25.9]	25.3[24.0]	−6.1[−9.7]

[a]Energies in brackets include single-point solvation determined using the CPCM (benzene) model. L corresponds to the indicated ligand in the table.

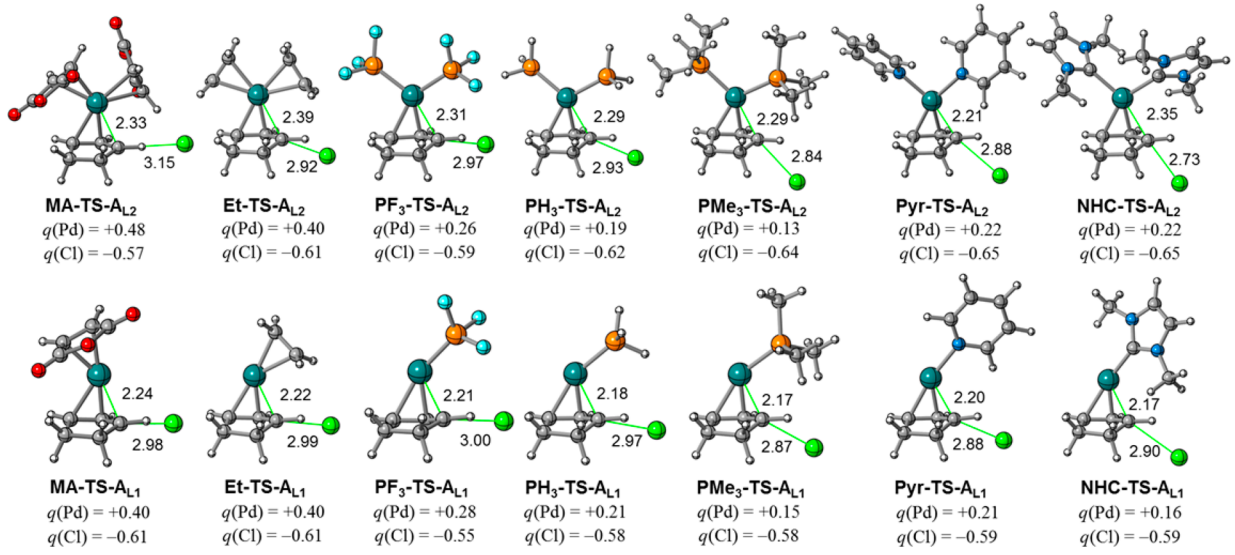

Figure 2. Transition state geometries for the *anti* pathway obtained at the TPSS-D3/def2-TZVP level. The listed values are distances in units of angstroms. Partial charges are VDD derived at the TPSS/TZ2P level.

dissociation transition states are only slightly higher in energy than the separated species and thus are not presented.

Association of the bis-ligated PdL_2 to the substrate (**RCT**) is downhill in free energy by ∼6−12 kcal/mol. Among all tested ligands, **RC-A$_{L2}$** is slightly favored over **RC-S$_{L2}$**, and there is a thermodynamic preference for having two ligands rather than one. In the gas phase, the *syn* pathway is always intrinsically favored irrespective of the ligation. The greatest preference for *syn* is observed with ligands that are generally electron-deficient. This preference is lowest for the **NHC** ligand (the most electron donating among the chosen ligands), for which the energy difference is only −0.7 kcal/mol ($\Delta G^{\ddagger}_{syn} - \Delta G^{\ddagger}_{anti}$).

dx.doi.org/10.1021/jo5020068 | J. Org. Chem. 2014, 79, 12136−12147

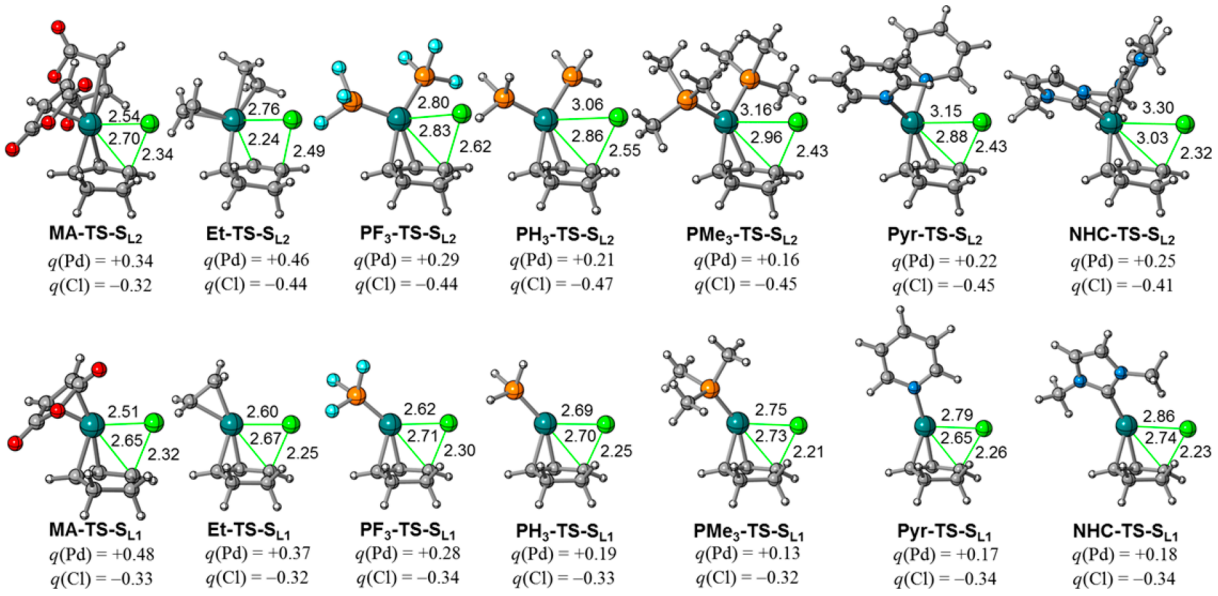

Figure 3. Transition state geometries for the *syn* pathway obtained at the TPSS-D3/def2-TZVP level. The listed values are distances in units of angstroms. Partial charges are VDD derived at the TPSS/TZ2P level.

The *syn* preference is higher for complexes with alkene ligands (**MA**, **Et**), which possess electron-withdrawing potential; these complexes can undergo ligand dissociation before oxidative addition. In general, the oxidative addition barriers decrease with increasing donor capacity of the ligands, more so for the *anti* than for the *syn* pathway.

The products of oxidative addition can exist as an equilibrium of the bis-ligated cationic (**PR$_{L2}$**) and the monoligated neutral (**PR$_{L1}$**) forms. In the case of **PH$_3$**, **PH$_3$-PR$_{L2}$** and **PH$_3$-PR$_{L1}$** may interconvert with a gas-phase barrier of 4.8 kcal/mol relative to **PH$_3$-PR$_{L2}$** (see the Supporting Information for the relevant transition state, **PH$_3$-TS$_{PR}$**). Electron-rich ligands favor **PR$_{L2}$**, whereas electron-deficient ligands tend to favor **PR$_{L1}$**. The **Pyr** ligand is an exception. The π-withdrawing capabilities of pyridine likely result in slight destabilization of the bound product because aromaticity in the pyridine ring is partially disrupted. This may also explain why **TS-A$_{L1}$** is unusually low in energy.

Solvation in a low dielectric (benzene, ε = 2.27) causes a preference for the *anti* pathway in most cases. In benzene, the **TS-A$_{L2}$** barriers decrease by 13 kcal/mol on average, compared with only 3 kcal/mol for **TS-S$_{L2}$**, causing an increase in the preference for *anti* addition. Similar trends can be observed upon comparing **TS-A$_{L1}$** with **TS-S$_{L1}$**. Clearly solvation can have a large influence, especially for the *anti* pathway. This is not surprising since classical S$_N$2 reactions are highly dependent on the solvent medium.[6b,31] The importance of solvation has also been demonstrated in the oxidative addition of unactivated alkyl chlorides, where the preference for front side versus back side attack can be fairly sensitive to the solvent medium.[7b]

For *anti* type pathways, having two ligands rather than one is consistently preferred by a significant energetic margin.[32] The transition states for the monoligated cases are noticeably *later* than those of the bis-ligated cases, as indicated by the Pd−C and C−Cl distances (Figure 2). Possessing only one ligand bound to the palladium center appears to be insufficient for supporting a facile dissociation of chloride. Complexes with electron-rich ligands require less bond elongation to reach the transition state. The strongly electron-donating **NHC** ligand leads to a noticeably earlier transition state than the other ligands.

Trends in the extent of reaction are less clear for the *syn* pathway than for the *anti* pathway. In the monoligated case, the C−Cl distance in the TS is shorter, indicating that less bond cleavage is necessary to reach the TS, whereas Pd−Cl bond formation is more advanced in the TS, as evidenced by the shorter Pd−Cl distances (Figure 3). These trends suggest that less C−Cl bond elongation is required in the monoligated examples because an earlier Pd−Cl bond formation is facilitated on account of the high degree of unsaturation at the palladium center. Once again, electron-rich ligands lead to earlier transition states, consistent with lower reaction barriers.

As indicated by the partial atomic charges, the *anti* pathway requires greater charge separation in the TS than the *syn* pathway for both ligation modes. Thus, it would seem appropriate to describe the *anti* pathway in terms of the dissociation of a chloride anion and the *syn* pathway in terms of the migration of a chlorine atom because chlorine experiences significantly less charge buildup in the *syn* transition states. The charge on the chlorine does not vary much across the ligand set within each pathway and ligation mode. Furthermore, the C−Cl bond elongation in the transition state is less for electron-rich ligands. Overall, the ease of the reaction may be viewed as being directly related to the capacity of the ligand to facilitate the transfer of a predefined amount of negative charge from the PdL$_n$ fragment to the dissociating or migrating chlorine atom.

Moreover, the additional charge separation caused by the presence of a dielectric is greater in the *anti* TS than in the *syn* TS. For example, the difference between the Hirshfeld charge on the chlorine atom in the gas phase and in a low dielectric (ε = 2.27) is Δq = 0.10 (−0.64 vs −0.74) for **PH$_3$-TS-A$_{L2}$** and Δq = 0.05 (−0.43 vs −0.48) for **PH$_3$-TS-S$_{L2}$**. The additional charge stabilization in the *anti* pathway may account for the resulting preference for *anti* addition with solvation for electron-rich ligands.

Comparison of the *syn* and *anti* Mechanisms. There are some noteworthy mechanistic differences between the *syn* and *anti* pathways. The *anti* pathway appears to follow an S$_N$2

dx.doi.org/10.1021/jo5020068 | J. Org. Chem. 2014, 79, 12136−12147

type mechanism, with the dissociated chloride atom eventually reassociating with the palladium atom along the reaction path.[33] The barrier is lowered with electron-rich relative to electron-deficient ligands.

The *syn* pathway also experiences a decrease in the activation barrier with increasingly electron-donating ligands but follows a mechanism that more closely adheres to an S_N1 type, in which the chlorine atom interacts with the palladium atom.[7b,34] The direct product, as revealed from IRC calculations, using $\mathbf{PH_3}$ as a representative example, is the η^3 product $\mathbf{PH_3}$-$\mathbf{PR_{L2}}$ (Figure 4). Alternatively, the formation of the η^1 product $\mathbf{PH_3}$-$\mathbf{PR_{\eta 1}}$

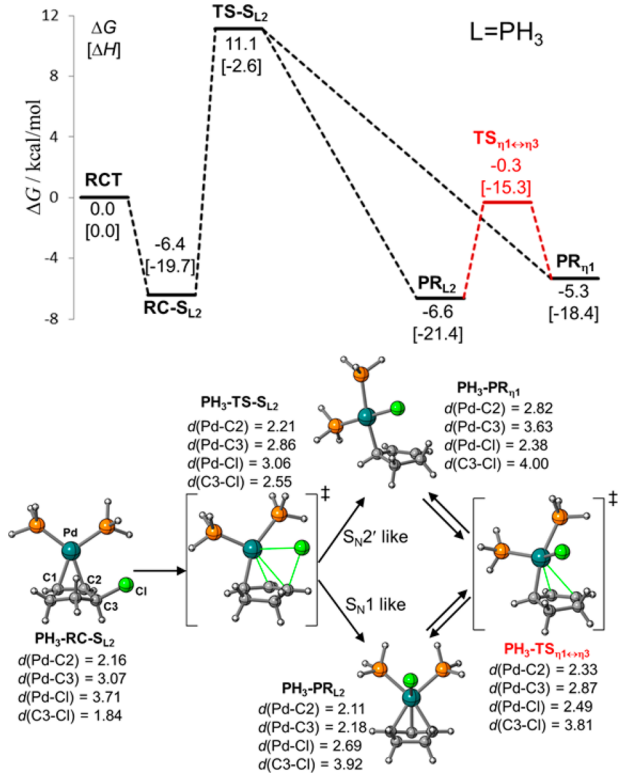

Figure 4. Gas-phase free energy profile (enthalpies in brackets) for the $\mathbf{PH_3}$-$\mathbf{TS}$-$\mathbf{S_{L2}}$ pathway. Energies are computed at the B2PLYP-D3/def2-TZVPP//TPSS-D3/def2-TZVP level. Distances are given in angstroms.

may also be envisioned, but a transition state for its direct formation from $\mathbf{PH_3}$-$\mathbf{RC_{L2}}$ could not be located despite an exhaustive search. The η^1 product does correspond to a stable minimum that may undergo a facile $\eta^1 \rightarrow \eta^3$ conversion to $\mathbf{PH_3}$-$\mathbf{PR_{L2}}$ via $\mathbf{PH_3}$-$\mathbf{TS_{\eta 1 \leftrightarrow \eta 3}}$. Geometrically, $\mathbf{PH_3}$-$\mathbf{TS}$-$\mathbf{S_{L2}}$ has some η^1 character judging from the Pd−C2 distance in $\mathbf{PH_3}$-$\mathbf{TS}$-$\mathbf{S_{L2}}$ (2.21 Å), which is greater than that in the η^3 adduct $\mathbf{PH_3}$-$\mathbf{PR_{L2}}$ (2.11 Å) and the reactant complex $\mathbf{PH_3}$-$\mathbf{RC_{L2}}$ (2.16 Å). Hence, it seems likely that $\mathbf{PH_3}$-$\mathbf{TS}$-$\mathbf{S_{L2}}$ connects three stationary points ($\mathbf{PH_3}$-$\mathbf{RC}$-$\mathbf{S_{L2}}$, $\mathbf{PH_3}$-$\mathbf{PR_{L2}}$, and $\mathbf{PH_3}$-$\mathbf{PR_{\eta 1}}$) and thus represents a bifurcation on the potential energy surface toward both the η^1 and η^3 products, in which the reaction coordinates for the oxidative addition ($\mathbf{TS}$-$\mathbf{S_{L2}}$) and the $\eta^1 \leftrightarrow \eta^3$ isomerization ($\mathbf{TS_{\eta 1 \leftrightarrow \eta 3}}$) are close to being orthogonal.[35] The thermodynamic preference for the η^3 product creates a dynamic preference (perturbation of the valley ridge inflection point) for $\mathbf{PH_3}$-$\mathbf{PR_{L2}}$.[36] Therefore, the mechanism can be regarded as a composite of S_N1 and S_N2' with greater S_N1 like character.

Fragment Analysis. The origin of the selectivity across the chosen ligand set was investigated by various computational techniques using fragment-based energy decomposition analysis. A representative case is illustrated for bis-ligation with $\mathbf{PH_3}$ in Table 2, which includes a pictorial definition of the energy components. Table 2 lists the components of the binding energy ΔE, the overall charge transfer from the Pd fragment to the allylic chloride fragment, the overlap between the HOMO of the Pd fragment and the LUMO of the allylic chloride fragment $\langle \mathbf{1}_{\mathrm{HOMO}} | \mathbf{2}_{\mathrm{LUMO}} \rangle$, and their orbital energies $\varepsilon(\mathbf{1}_{\mathrm{HOMO}})$ and $\varepsilon(\mathbf{2}_{\mathrm{LUMO}})$. The slight preference for *anti* association arises primarily from the increased distortion of the allylic chloride fragment in *syn* association that serves to relieve excess Pauli repulsion between the chlorine atom and the $Pd(PH_3)_2$ fragment. This additional distortion leads to the lowering of the LUMO energy $\varepsilon(\mathbf{2})$ of the allylic chloride fragment and to a slight increase in the orbital overlap with the HOMO of the $Pd(PH_3)_2$ fragment, as compared to the case of *anti* association. Consequently, there are slightly enhanced orbital and electrostatic interactions for *syn* association as well as an increased overall charge transfer (Δq).

The variation in the transition state properties is much greater than that in the reactant complexes. The interaction energies with $Pd(PH_3)_2$ are nearly identical in the transition states. The difference of 10.9 kcal/mol between $\mathbf{PH_3}$-$\mathbf{TS}$-$\mathbf{A_{L2}}$ and $\mathbf{PH_3}$-$\mathbf{TS}$-$\mathbf{S_{L2}}$ almost exclusively arises from the difference in the distortion energy ($\Delta\Delta E_{\mathrm{dist}}$ = 11.2 kcal/mol), which is primarily due to the distortion between the allylic chloride components ($\Delta\Delta E_{\mathrm{d2}}$ = 12.8 kcal/mol). Hence, distortion effects cause a large preference for $\mathbf{PH_3}$-$\mathbf{TS}$-$\mathbf{S_{L2}}$, which is, however, reduced to ∼3 kcal/mol after including the electrostatic and orbital interactions. While one might be hesitant to extract detailed conclusions from the difference in interaction components between geometrically quite different structures, one may still conclude with confidence that the *syn* pathway is favored over the *anti* pathway on account of the large distortion difference favoring *syn*. This conclusion is a little vexing when considering the charge transfer, the $\langle \mathbf{1}_{\mathrm{HOMO}} | \mathbf{2}_{\mathrm{LUMO}} \rangle$ overlap, and the frontier orbital energy difference, which all seem to favor $\mathbf{PH_3}$-$\mathbf{TS}$-$\mathbf{A_{L2}}$. This point will be elaborated further in a separate section as further orbital interactions appear to be contributing.

The monoligated case with $Pd-PH_3$ (Table 3) is similar to the bis-ligated case with $Pd(PH_3)_2$ (Table 2). The interaction in the reactant complexes is weakened, but this is compensated by requiring less distortion in the $Pd-PH_3$ fragment, as expected for a linear monoligated complex. The orbital interactions are diminished since the $Pd-PH_3$ moiety is positioned such that there is rather little overlap of its HOMO with the LUMO of the allylic component (0.096 vs. 0.244 in the bis-ligated case).

For $Pd-PH_3$, the preference for the *syn* pathway is significantly enhanced ($\Delta\Delta E$ = 20.3 kcal/mol). The interaction components favoring $\mathbf{PH_3}$-$\mathbf{TS}$-$\mathbf{A_{L1}}$ by 12.2 kcal/mol are completely overwhelmed by the distortion components favoring $\mathbf{PH_3}$-$\mathbf{TS}$-$\mathbf{S_{L1}}$ by 31.4 kcal/mol. The overall charge transfer to the allylic chloride is also comparably low on the monoligated *syn* pathway, suggesting that charge transfer to $Pd-PH_3$ is significant.

There is little difference in the nature of the reactant complex across all ligands explored.[37] The most stabilizing component of the interaction is the electrostatic one. The largest difference is observed with η^2 alkene ligands. The charge transfer and the

dx.doi.org/10.1021/jo5020068 | J. Org. Chem. 2014, 79, 12136−12147

Table 2. Energy Profile for Bis-Ligation with PH_3[a]

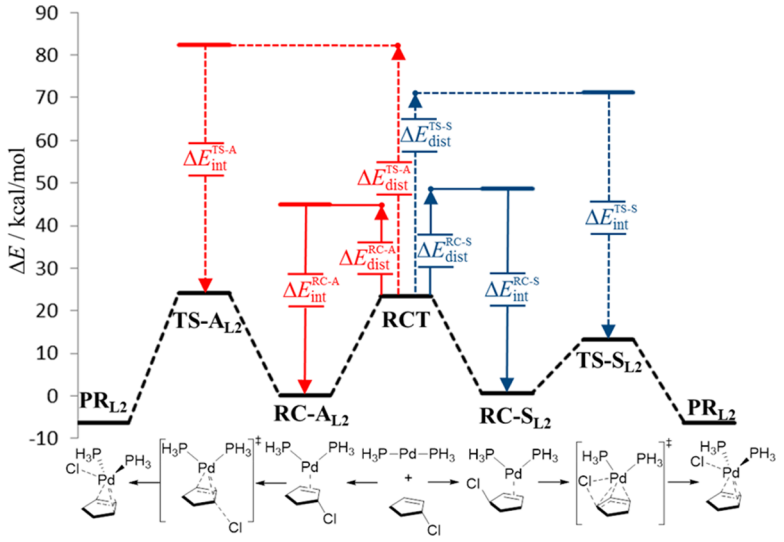

	ΔE	ΔE_{dist}[d]	ΔE_{int}	ΔE_{Pauli}	ΔE_{elec}	ΔE_{orb}	ΔE_{disp}	$\Delta E_d(\mathbf{1})$[b]	$\Delta E_d(\mathbf{2})$[c]	Δq[e]	$\langle \mathbf{1}_{HOMO}\vert\mathbf{2}_{LUMO}\rangle$[f]	$\varepsilon(\mathbf{1}_{HOMO})$[g]	$\varepsilon(\mathbf{2}_{LUMO})$
RC-A_{L2}	−23.38	21.64	−45.02	152.68	−120.81	−70.04	−6.85	12.97	8.67	0.152	0.244	−4.09	−1.88
RC-S_{L2}	−22.68	25.27	−47.95	164.16	−127.81	−76.46	−7.84	13.47	11.80	0.160	0.257	−4.04	−1.73
TS-A_{L2}	0.73	59.07	−58.34	175.93	−119.70	−107.16	−7.41	15.00	44.07	0.454	0.216	−3.94	−4.53
TS-S_{L2}	−10.20	47.90	−58.10	180.25	−120.32	−109.68	−8.35	15.76	32.14	0.354	0.159	−3.90	−3.95

[a]Numerical values are given for the energy components of the interaction energy, the overall charge transfer between the fragments Δq, the overlap between the HOMO of the Pd−PH_3 fragment ($\mathbf{1}_{HOMO}$) and the LUMO of the allylic fragment ($\mathbf{2}_{LUMO}$) $\langle \mathbf{1}_{HOMO}\vert\mathbf{2}_{LUMO}\rangle$, and the corresponding orbital energies $\varepsilon(\mathbf{1})$ and $\varepsilon(\mathbf{2})$. [b]Distortion energy of the Pd−PH_3 fragment. [c]Distortion energy of the allylic chloride fragment. [d]$\Delta E_{dist} = \Delta E_d(\mathbf{1}) + \Delta E_d(\mathbf{2})$. [e]NBO overall charge transfer. [f]Orbital overlap between the HOMO of the $Pd(PH_3)_2$ fragment ($\mathbf{1}_{HOMO}$) and the LUMO of the allylic chloride fragment ($\mathbf{2}_{LUMO}$). [g]Orbital energy of the $\mathbf{1}_{HOMO}$ fragment orbital in eV.

Table 3. Energy Profile for Monoligation with PH_3[a]

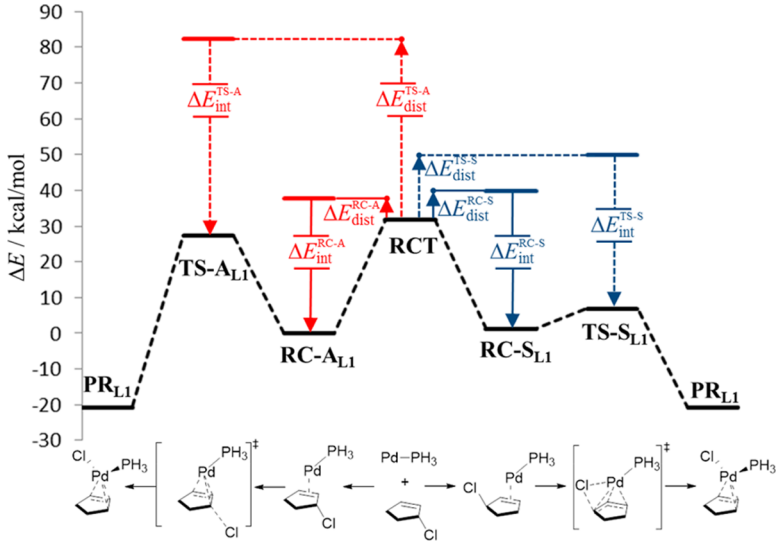

	ΔE	ΔE_{dist}[d]	ΔE_{int}	ΔE_{Pauli}	ΔE_{elec}	ΔE_{orb}	ΔE_{disp}	$\Delta E_d(\mathbf{1})$[b]	$\Delta E_d(\mathbf{2})$[c]	Δq[e]	$\langle \mathbf{1}_{HOMO}\vert\mathbf{2}_{LUMO}\rangle$[f]	$\varepsilon(\mathbf{1}_{HOMO})$[g]	$\varepsilon(\mathbf{2}_{LUMO})$
RC-A_{L1}	−31.78	5.91	−37.69	130.73	−105.86	−57.98	−4.58	1.04	4.87	0.091	0.096	−4.41	−1.63
RC-S_{L1}	−30.53	8.14	−38.67	138.01	−108.68	−62.89	−5.11	0.95	7.19	0.100	0.139	−4.42	−1.50
TS-A_{L1}	−4.54	50.52	−55.06	185.90	−125.79	−109.51	−5.66	3.42	47.10	0.432	0.152	−4.29	−4.60
TS-S_{L1}	−24.83	18.08	−42.91	173.95	−120.85	−90.10	−5.91	0.64	17.44	0.165	0.128	−4.45	−3.08

[a]Numerical values are given for the energy components of the interaction energy, the overall charge transfer between the fragments Δq, the overlap between the HOMO of the Pd−PH_3 fragment ($\mathbf{1}_{HOMO}$) and the LUMO of the allylic fragment ($\mathbf{2}_{LUMO}$) $\langle \mathbf{1}_{HOMO}\vert\mathbf{2}_{LUMO}\rangle$, and the corresponding orbital energies $\varepsilon(\mathbf{1})$ and $\varepsilon(\mathbf{2})$. [b]Distortion energy of the Pd−PH_3 fragment. [c]Distortion energy of the allylic chloride fragment. [d]$\Delta E_{dist} = \Delta E_d(\mathbf{1}) + \Delta E_d(\mathbf{2})$. [e]NBO overall charge transfer. [f]Orbital overlap between the HOMO of the $Pd(PH_3)_2$ fragment $\mathbf{1}_{HOMO}$ and the LUMO of the allylic chloride fragment $\mathbf{2}_{LUMO}$. [g]Orbital energy of the $\mathbf{1}_{HOMO}$ fragment orbital in electron volts (eV).

dx.doi.org/10.1021/jo5020068 | J. Org. Chem. 2014, 79, 12136−12147

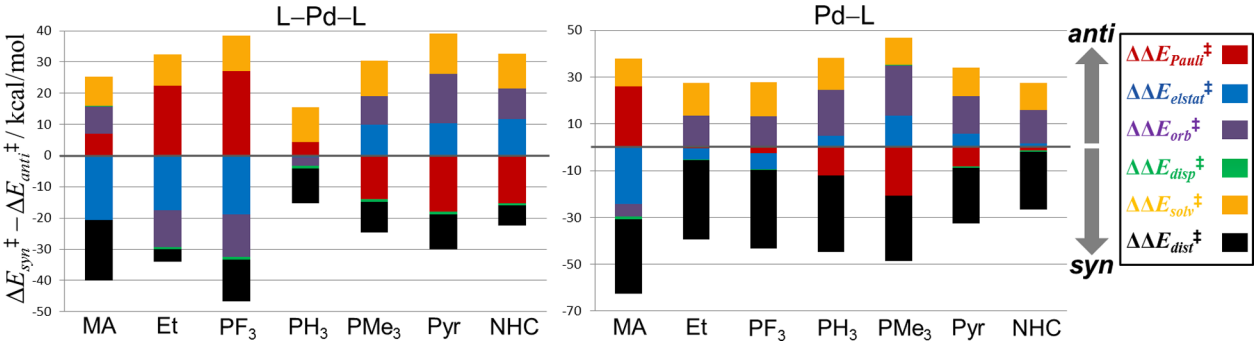

Figure 5. Differences in energy components plotted as $\Delta E_{syn}^{\ddagger} - \Delta E_{anti}^{\ddagger}$. Positive values favor *anti*, whereas negative values favor *syn*. The plot on the left is for bis-ligation PdL_2, and the plot on the right is for monoligation Pd–L. The solvation energy difference ($\Delta\Delta E_{solv}^{\ddagger}$) is obtained at the CPCM(benzene)-TPSS-D3/def2-TZVP level.

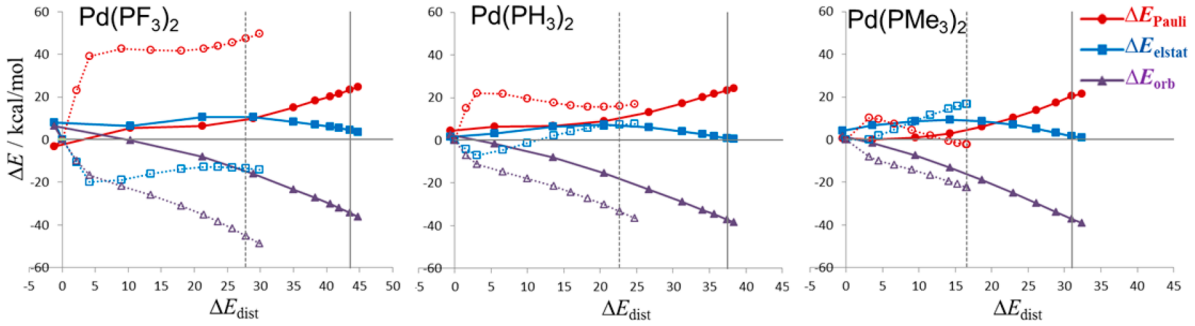

Figure 6. EDA along the reaction coordinate projected along the distortion energy ΔE_{dist} under bis-ligation. Energy terms are given relative to their values in the reactant complex. The solid lines represent the *anti* pathway, and the dotted lines represent the *syn* pathway. The gray vertical lines mark the transition state locations (dotted, *syn*; solid, *anti*).

$\langle \mathbf{1}_{HOMO}|\mathbf{2}_{LUMO}\rangle$ overlap increase significantly with increasing HOMO of the Pd fragment (more electron-rich ligands).

Results for the remaining ligands are illustrated in Figure 5, which shows the differences between the interaction energy components in the *anti* and *syn* transition states ($\Delta E_{syn}^{\ddagger} - \Delta E_{anti}^{\ddagger}$) that govern the *syn*/*anti* preference. For bis-ligation, the stabilizing components (ΔE_{orb} and ΔE_{elstat}) for electron-rich ligands (**PMe_3**, **Pyr**, **NHC**) all reside in the positive region and thus favor the *anti* pathway. However, the combined Pauli repulsion (ΔE_{Pauli}) and distortion (ΔE_{dist}) components fully compensate for the attractive components, and the final result is a solid or slight preference for the *syn* pathway. The situation is reversed for electron-deficient ligands (**PF_3**, **Et**), where the stabilizing components favor the *syn* pathway, and the destabilizing components (ΔE_{Pauli} and ΔE_{dist}), the *anti* pathway. For the **MA** ligand, the orbital term (ΔE_{orb}) is more stabilizing in the *anti* pathway. This counterintuitive result can be explained by the fact that the *anti* pathway exhibits a much greater degree of distortion than the *syn* pathway, more so than for all of the other ligands. This unusually large amount of distortion causes greater orbital overlap for the **MA** case as compared to **PF_3** and **Et**.

Inclusion of the solvation energy causes a shift in the overall preference from *syn* to *anti* for electron-rich ligands and an appreciably diminished preference for *syn* for electron-deficient ligands. The solvation energy ($\Delta\Delta E_{solv}^{\ddagger}$ = 9–11 kcal/mol, ε = 2.27) does not contribute much to the variation in $\Delta\Delta E^{\ddagger}$ across the entire ligand set. As addressed in a prior section, solvation causes a greater degree of charge separation on the *anti* pathway, which likely results in stabilization of this pathway. Since the solvent effects on the *syn*/*anti* preference are rather uniform across the ligands investigated, we refrain from a more detailed discussion.

Interestingly, in the case of monoligation, the orbital interactions for all ligands (except **MA**) favor the *anti* side, whereas both destabilizing components (ΔE_{Pauli} and ΔE_{dist}) favor the *syn* side, with the latter being overwhelmingly preferred overall energetically. Solvation does favor *anti* but not enough to shift the overall preference from *syn* to *anti*, even for the most electron-rich ligands. These results are counterintuitive in that the *syn* pathway would be expected to have similar orbital interactions because the palladium atom is highly unsaturated and should strongly benefit from association with the migrating chlorine atom (relative to the *anti* pathway). However, the substantial difference in distortion energy renders conclusions drawn from comparison of the interaction components suspect since the transition states are located at very different points along their respective reaction coordinates (i.e., *anti* much later than *syn*). This calls for inspection of the interaction components along the reaction coordinate to circumvent the problems inherent to a single-point analysis.[23]

Examination along the IRC: Interaction EDA. While comparison of the energy components at the transition states provides valuable insight when the changes in distortion are similar, this is not necessarily the case when these changes are very large. More tenable insights may then be obtained from an examination of the variations along the reaction coordinate. Here, the reaction coordinate is projected along the distortion energy[38] in view of the requirement that at the transition state, $d\Delta E_{int}/d\Delta E_{dist} = -1$. The distortion profiles for properties related to the interaction term therefore directly influence the degree of distortion required to reach the point where an

dx.doi.org/10.1021/jo5020068 | J. Org. Chem. 2014, 79, 12136–12147

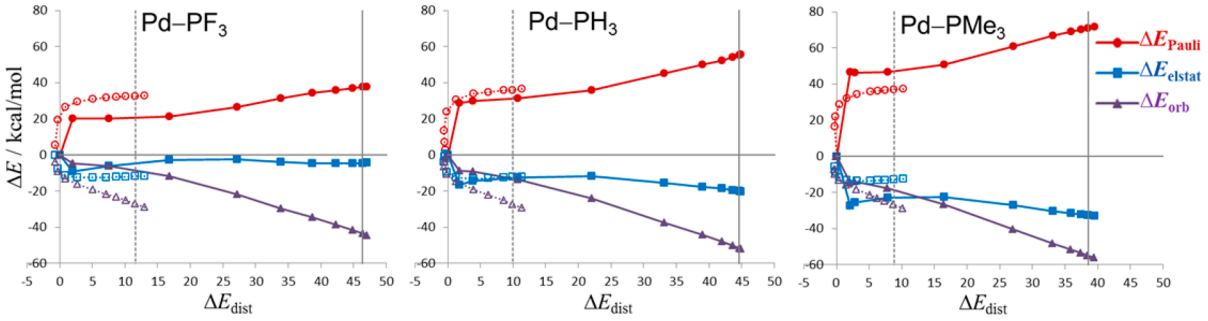

Figure 7. EDA along the reaction coordinate projected along the distortion energy ΔE_{dist} under monoligation. Energy terms are given relative to their values in the reactant complex. The solid lines represent the *anti* pathway, and the dotted lines represent the *syn* pathway. The gray vertical lines mark the transition state locations (dotted, *syn*; solid, *anti*).

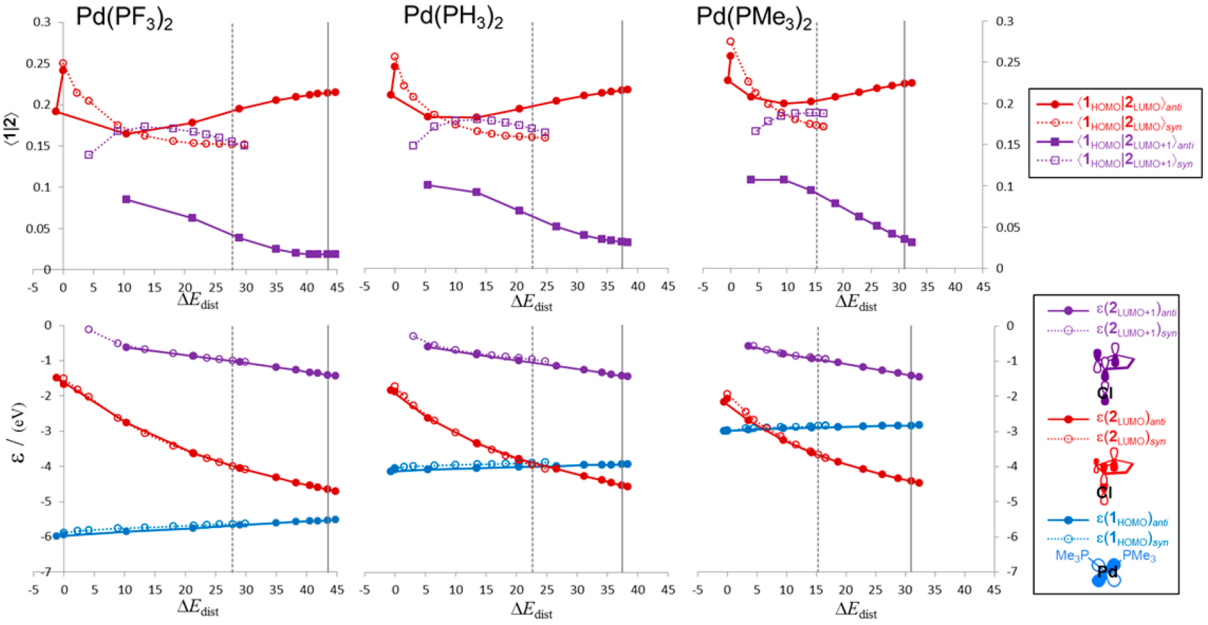

Figure 8. Top: Orbital overlap plotted as a function of the overall distortion energy ΔE_{dist} (kcal/mol) for the *syn* and *anti* pathways under bis-ligation. Bottom: Orbital energies plotted as a function of the overall distortion energy ΔE_{dist} (kcal/mol). The LUMO and LUMO+1 of the allylic fragment are colored in red and purple, respectively, and the HOMO of the PdL_2 fragment is colored in blue. The *anti* and *syn* pathways are depicted in solid and dotted lines, respectively.

infinitesimal additional distortion is compensated by an equal amount of additional interaction (the transition state).

Distortion profiles of the interaction components under bis-ligation are presented in Figure 6. For the sake of clarity, the dispersion term ΔE_{disp} is not displayed, as it does not contribute measurably to the selectivity. The electrostatic term ΔE_{elstat} undergoes little change in the *anti* pathway for all three ligands and exhibits a broad maximum. The initial increase in electrostatic repulsion for the *anti* pathway is caused by a considerable decrease in the Pd−C distance without a comparable increase in the C−Cl distance. The C−Cl separation becomes significant enough after 15−20 kcal/mol of distortion to compensate for the decreasing Pd−C distance. Conversely, in the *syn* pathway for $\mathbf{PF_3}$, an electrostatic attraction is present over the course of the reaction, whereas the fragments with $\mathbf{PH_3}$ and $\mathbf{PMe_3}$ ligands primarily experience an electrostatic repulsion (relative to the reactant complex). This difference is consistent with the VDD partial charges on the Pd atoms of the isolated fragments in the reactant complexes, in which the charge on Pd becomes more positive with decreasing ligand donating strength: $q(\mathrm{Pd})_{\mathbf{PF_3}} = 0.15e$, $q(\mathrm{Pd})_{\mathbf{PH_3}} = 0.04e$, $q(\mathrm{Pd})_{\mathbf{PMe_3}} = -0.03e$. The chlorine atom accumulates negative charge in the course of the reaction and thus engages in an electrostatic attraction with the partially positive Pd atom of the $Pd(PF_3)_2$ fragment.

The orbital term ΔE_{orb} is always more favored for the *syn* pathway, although the preference is greatly diminished with $\mathbf{PMe_3}$. This finding is in contrast to the commonly held view that *anti* engages in stronger overall frontier orbital overlap.[39] It is again noteworthy that inspection at the transition state would result in the misleading conclusion that orbital interactions are similar or greater for the *anti* pathway in the case of $\mathbf{PMe_3}$; this interpretation neglects the ∼15 kcal/mol difference in distortion energy (ΔE_{dist}) at the TS's. The lower charge transfer per unit distortion for *syn* vs *anti*, especially for the $\mathbf{PF_3}$ case, would suggest that donation from the allylic fragment to the PdL_2 fragment in the *syn* pathway is contributing significantly to the enhanced orbital interactions present for *syn*.[40]

The monoligation pathways yield interaction/distortion profiles exhibiting very different behavior than those for the bis-ligation pathways (Figure 7). The *syn* energy components

dx.doi.org/10.1021/jo5020068 | J. Org. Chem. 2014, 79, 12136−12147

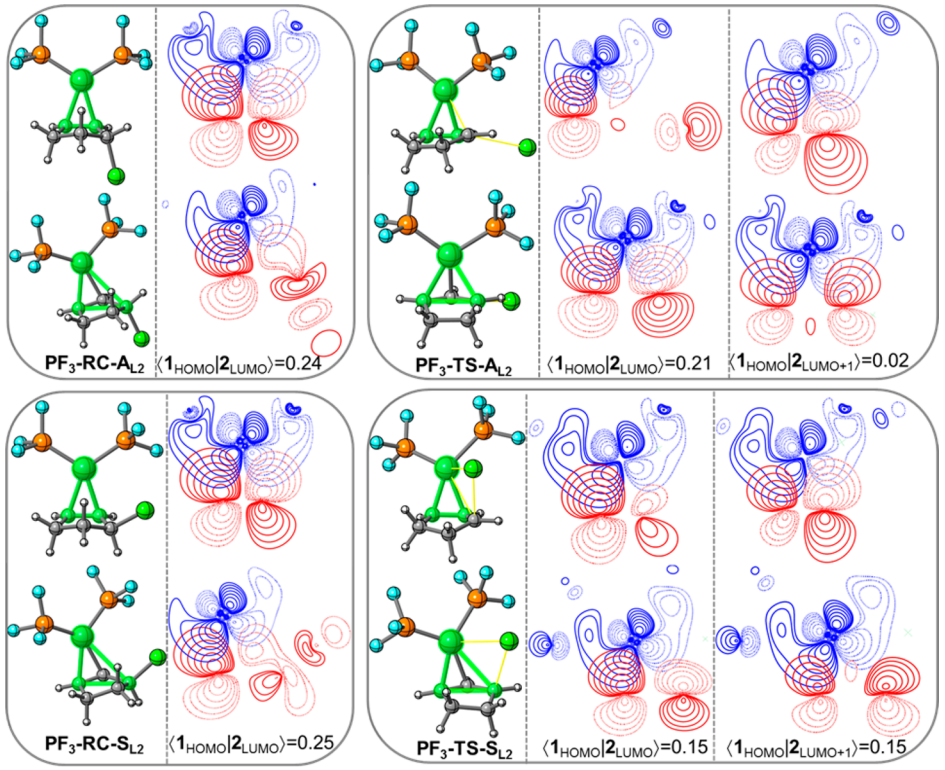

Figure 9. Contours of the HOMO (blue) of $Pd(PF_3)_2$ superimposed on to the LUMO and the LUMO+1 (red) of the allylic chloride moiety for the reactant complexes and the corresponding transition states on the *syn* and *anti* pathways. The three atoms used for the contour alignment are highlighted in green. Two different perspectives are provided for each orbital interaction displayed. Opposing phases are differentiated by solid and dotted lines.

change rapidly during the initial stages of the reaction. The Pauli (ΔE_{Pauli}) and electrostatic (ΔE_{elstat}) terms level off very early. The orbital term (ΔE_{orb}) continues its descent until the TS is reached. Generally, the *syn* pathway is influenced very little by ligand alterations. In contrast, the *anti* pathway undergoes only a small gradual change in the interaction components along the distortion profile. Compared to the *anti* pathway with bis-ligation, there is much greater Pauli repulsion. The greater repulsion is reflected in the requirement for enhanced propinquity between the Pd and the C−Cl σ^* orbitals to achieve orbital contact sufficient for C−Cl cleavage (Figure 3). Compared to bis-ligation, the electrostatic interaction (ΔE_{elstat}) is enhanced as a consequence of the decreased separation.

Frontier Orbital Considerations. The orbital interactions under the more common bis-ligation mode were analyzed in greater detail for conceptualizing the difference in orbital interaction terms (ΔE_{orb}) between *syn* and *anti* with alterations in ligand electronics. Particular points that should be highlighted as to how orbital interactions are more enhanced in the *syn* pathway include (i) which pathway is more conducive to charge transfer from the Pd fragment to the allylic fragment, (ii) which pathway is more conducive to charge transfer from the allylic fragment to the Pd fragment, and (iii) the role of the ligand in influencing the magnitude of the orbital preferences.

The overlaps of the HOMO on the PdL_2 fragment with the LUMO and LUMO+1 on the allylic fragment were analyzed as a function of the distortion (Figure 8). The $\langle \mathbf{1}_{HOMO}|\mathbf{2}_{LUMO}\rangle_{syn}$ overlap decays exponentially until the TS is reached on the *syn* pathway. In contradistinction, the corresponding $\langle \mathbf{1}_{HOMO}|\mathbf{2}_{LUMO}\rangle_{anti}$ overlap on the *anti* path initially decreases and then begins to increase at an early stage of the reaction through the TS. The change in overlap with different ligands does not appear to be significant. The $\langle \mathbf{1}_{HOMO}|\mathbf{2}_{LUMO+1}\rangle$ overlap is much greater on the *syn* pathway than on the *anti* pathway. In the latter case, it decreases asymptotically to zero.

As anticipated, the orbital energies increase for the HOMO and decrease for the LUMO as the components are distorted. There is very little difference in the orbital energies between the *anti* and *syn* pathways (closed and open circles, respectively). The $\mathbf{1}_{HOMO}$ orbital energy of the PdL_2 fragment does not change much with the distortion energy. There is a significant shift in the PdL_2 HOMO energy with more electron-rich ligands, to the extent that the orbital interaction is best characterized in terms of charge transfer for the largest part of the reaction with $Pd(PMe_3)_2$. The LUMO exhibits the largest energy change with distortion accordant with the requisite C−Cl elongation (C−Cl σ^* lowering). The LUMO+1 is ∼2−3 eV higher in energy than the LUMO, but it is still low enough relative to the HOMO to provide a substantial contribution to the overall orbital term ΔE_{orb}.

Collectively, the orbital overlap and the corresponding orbital energies for the PdL_2 HOMO and the allylic LUMO and LUMO+1 present a convincing case for greater frontier orbital interactions on the *syn* pathway. The rationale behind the differences in overlap becomes clearer upon inspection of a superimposition of the relevant orbitals, as illustrated for $Pd(PF_3)_2$ (Figure 9). Both the reactant complexes exhibit similar $\langle \mathbf{1}_{HOMO}|\mathbf{2}_{LUMO}\rangle$ overlap, which is slightly larger for **RC-S$_{L2}$** due to slightly greater distortion in the allylic fragment. The $\langle \mathbf{1}_{HOMO}|\mathbf{2}_{LUMO}\rangle$ overlap is slightly smaller in **TS-A$_{L2}$** than in the

dx.doi.org/10.1021/jo5020068 | J. Org. Chem. 2014, 79, 12136−12147

associated reactant complex **RC-A$_{L2}$** by virtue of the larger distance between the carbon atoms with the largest LUMO coefficients (p-like orbitals of an allyl cation in **TS-A$_{L2}$** versus π^* orbitals of the alkene in **RC-A$_{L2}$**). This larger distance creates a slight mismatch with the HOMO on Pd(PF$_3$)$_2$. In contrast, the $\langle \mathbf{1}_{HOMO}|\mathbf{2}_{LUMO}\rangle$ overlap in **TS-S$_{L2}$** is apparently diminished considerably. The alignment is disrupted by the occupied orbitals on the migrating Cl atom, resulting in only one of the lobes of the $\mathbf{2}_{LUMO}$ engaging in strong overlap with the $\mathbf{1}_{HOMO}$.

In contrast, the $\langle \mathbf{1}_{HOMO}|\mathbf{2}_{LUMO+1}\rangle$ overlap differs more between the *anti* and *syn* pathways. In **TS-A$_{L2}$**, it is very small (0.02) because of significant antibonding interactions. Conversely, the overlap is higher (0.15) in **TS-S$_{L2}$** since the antibonding interactions between the HOMO (at Pd(PF$_3$)$_2$) and LUMO+1 (at the terminal carbon of the allyl moiety) are largely avoided and there is larger constructive overlap with the central carbon of the allyl moiety (compared with **TS-A$_{L2}$**).

While this analysis sheds light on the dominant orbital interactions between the fragments for the *syn* pathway, it does not account for the diminishing orbital preference for *syn* upon introduction of more electron-donating ligands. Another cause for the diminishing orbital preference may be donation from the migrating chlorine atom to the PdL$_2$ fragment. This type of interaction would conform with the notion that the energies of the unoccupied orbitals on the PdL$_2$ fragment should be sensitive to the ligand electronics.

The LUMO and LUMO+1 of the Pd(PF$_3$)$_2$ fragment are displayed in Figure 10. The HOMO of the allylic chloride

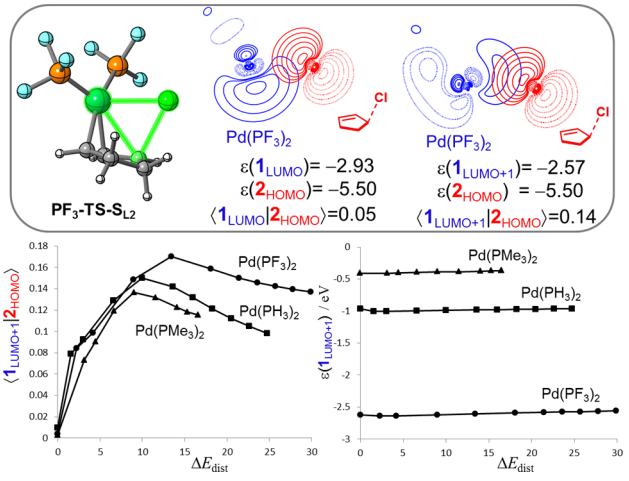

Figure 10. Contours of the LUMO and LUMO+1 (blue) of Pd(PF$_3$)$_2$ superimposed on to the HOMO (red) of the allylic chloride for the *syn* transition state. The overlap and the corresponding orbital energies (eV) are listed. The three atoms used for the contour alignment are highlighted in green. Opposing phases are differentiated by solid and dotted lines. The bottom panel shows the distortion profiles of the $\langle \mathbf{1}_{LUMO+1}|\mathbf{2}_{HOMO}\rangle$ overlap and the $\mathbf{1}_{LUMO+1}$ orbital energy.

fragment is primarily an isolated 3p orbital of the migrating chlorine atom. The overlap with the LUMO of the Pd(PF$_3$)$_2$ fragment (mostly Pd 5s) is only 0.05, whereas the overlap with the LUMO+1 (admixture of 4p Pd and 2p P) is 0.14. This latter overlap is likely to contribute most to the Pd−Cl bonding interaction. According to a natural orbitals of chemical valence (NOCV)[41] analysis, the Pd−Cl interaction corresponds to the second most dominant orbital interaction representing charge transfer from the allylic fragment to Pd(PF$_3$)$_2$.[42] Moreover, the orbital energy of the LUMO+1 on the PdL$_2$ fragment is lowered significantly as the ligand is more withdrawing ($\mathbf{1}_{LUMO+1}(\mathbf{PF_3})$ = −2.5 eV; $\mathbf{1}_{LUMO+1}(\mathbf{PMe_3})$ = −0.5 eV), which results in a strengthening of this interaction with withdrawing ligands. Similar to the HOMO energy of PdL$_2$, the LUMO+1 energy changes only slightly with the overall distortion, which is consistent with most of the distortion change occurring within the allylic chloride fragment. The overlap among the three ligands begins to separate at around 10 kcal/mol of overall distortion energy (Figure 10).

In summary, the overall orbital preference with electron-rich ligands arises from a comparably greater $\langle \mathbf{1}_{HOMO}|\mathbf{2}_{LUMO+1}\rangle$ interaction in the *syn* pathway that compensates for the somewhat greater $\langle \mathbf{1}_{HOMO}|\mathbf{2}_{LUMO}\rangle$ interaction in the *anti* pathway. Moreover, the combined overlap and orbital energy differences between the allylic chloride HOMO (3p) and the Pd(PF$_3$)$_2$ LUMO+1 can be used to rationalize the decrease in the orbital interaction difference between the *anti* and *syn* pathways with ligands of increasing electron-donating strength.[43]

CONCLUSIONS

The origin of the *syn* and *anti* preference in the oxidative addition of PdL$_n$ by 3-chloro-cyclopentene was investigated using DFT. In the gas phase, the *syn* pathway is preferred for all ligands studied, although the preference diminishes significantly with increasing electron-donating strength of the ligand. Bis-ligation is preferred for η^1 bound ligands, whereas under monoligation, the *syn* pathway is favored overall for η^2 bound alkene ligands. In a low dielectric medium, there is a tendency to shift the intrinsic preference from the *syn* pathway to the *anti* pathway for electron-rich ligands.

An interaction/distortion analysis demonstrates that, overall, the *anti* pathway requires a significantly larger degree of distortion than the *syn* pathway, which is predominantly manifest in the allylic chloride fragment. The difference in distortion energies is even more pronounced in the monoligation mode, as one ligand is insufficient for attaining dissociation of chloride with less than a prohibitive energetic cost.

The component of the interaction energy that influences the selectivity most is the electrostatic component (ΔE_{elstat}). It is most sensitive toward the electronics of the ligand. The electrostatic preference for *syn* is largely attributed to the attraction between the electropositive palladium and the migrating chlorine atom that is strengthened with electron-deficient ligands. In addition, the diminishing preference for *syn* with electron-donating ligands is related to the electrostatic repulsion between the electron-rich palladium center and the migrating electronegative chlorine atom.

The overall orbital preference for *syn* is manifest in the ensuing interaction between the Pd and Cl atoms along the reaction path. This interaction is enhanced with electron-deficient ligands on the Pd atom. The greater overall orbital preference for the *syn* pathway arises from the strong $\langle \mathbf{1}_{LUMO+1}|\mathbf{2}_{HOMO}\rangle_{syn}$ interaction (nonexistent in the *anti* pathway) and a large $\langle \mathbf{1}_{HOMO}|\mathbf{2}_{LUMO+1}\rangle_{syn}$ interaction (stronger than that in the *anti* case), which more than compensates for the greater $\langle \mathbf{1}_{HOMO}|\mathbf{2}_{LUMO}\rangle_{anti}$ interaction.

The analysis presented herein provides additional insight into the origin of selectivity preferences in palladium-catalyzed allylic alkylation. The results may prove to be useful in the design of novel ligands for palladium and other transition

dx.doi.org/10.1021/jo5020068 | J. Org. Chem. 2014, 79, 12136−12147

metals that are able to effect allylic alkylation for unique substrates.

■ ASSOCIATED CONTENT

Supporting Information

Cartesian coordinates, energies of all stationary points, intrinsic reaction coordinate diagrams, and additional analyses. This material is available free of charge via the Internet at http://pubs.acs.org.

■ AUTHOR INFORMATION

Corresponding Author

*Phone: +49(0)208/306-2150. Fax: +49(0)208/306-2996. E-mail: thiel@kofo.mpg.de.

Notes

The authors declare no competing financial interest.

■ ACKNOWLEDGMENTS

We are grateful to Prof. Dr. Nuno Maulide for helpful discussions. Financial support for this work was provided by the Max Planck Gesellschaft.

■ REFERENCES

(1) (a) Trost, B. M. *Tetrahedron* **1977**, *33*, 2615−2649. (b) Trost, B. M.; Van Vranken, D. L. *Chem. Rev.* **1996**, *96*, 395−422. (c) Trost, B. M.; Crawley, M. L. *Chem. Rev.* **2003**, *103*, 2921−2943. (d) Trost, B. M. *J. Org. Chem.* **2004**, *69*, 5813−5837. (e) Lu, Z.; Ma, S. M. *Angew. Chem., Int. Ed.* **2008**, *47*, 258−297.

(2) Kleimark, J.; Norrby, P.-O. *Top. Organomet. Chem.* **2012**, *38*, 65−94.

(3) Hegedus, L. S.; Darlington, W. H.; Russell, C. E. *J. Org. Chem.* **1980**, *45*, 5193−5196.

(4) (a) Hagelin, H.; Åkermark, B.; Norrby, P.-O. *Chem.—Eur. J.* **1999**, *5*, 902−909. (b) Johansson, C.; Lloyd-Jones, G.; Norrby, P.-O. *Tetrahedron: Asymmetry* **2010**, *21*, 1585−1592. (c) Kleimark, J.; Johansson, C.; Olsson, S.; Håkansson, M.; Hansson, S.; Åkermark, B.; Norrby, P.-O. *Organometallics* **2011**, *30*, 230−238.

(5) (a) Sakaki, S.; Nishikawa, M.; Ohyoshi, A. *J. Am. Chem. Soc.* **1980**, *102*, 4062−4069. (b) Goldfuss, B.; Kazmaier, U. *Tetrahedron* **2000**, *56*, 6493−6496. (c) Svensen, N.; Fristrup, P.; Tanner, D.; Norrby, P.-O. *Adv. Synth. Catal.* **2007**, *349*, 2631−2640.

(6) (a) Bickelhaupt, F. M.; Ziegler, T. *Organometallics* **1995**, *14*, 2288−2296. (b) Diefenbach, A.; Bickelhaupt, F. M. *J. Phys. Chem. A* **2004**, *108*, 8460−8466. (c) Gooβen, L. J.; Koley, D.; Hermann, H.; Thiel, W. *Chem. Commun.* **2004**, 2141−2143. (d) Senn, H. M.; Ziegler, T. *Organometallics* **2004**, *23*, 2980−2988. (e) Diefenbach, A.; de Jong, T. G.; Bickelhaupt, F. M. *J. Chem. Theory Comput.* **2005**, *1*, 286−298. (f) Ariafard, A.; Lin, Z. *Organometallics* **2006**, *25*, 4030−4033. (g) de Jong, T. G.; Bickelhaupt, F. M. *J. Chem. Theory Comput.* **2007**, *3*, 514−529. (h) de Jong, T. G.; Bickelhaupt, F. M. *ChemPhysChem* **2007**, *8*, 1170−1181. (i) Lam, K. C.; Marder, T. B.; Lin, Z. *Organometallics* **2007**, *26*, 758−760. (j) Legault, C. Y.; Garcia, Y.; Merlic, C. G.; Houk, K. N. *J. Am. Chem. Soc.* **2007**, *129*, 12664−12665.

(7) (a) Kurosawa, H.; Ogoshi, S.; Kawasaki, Y.; Murai, S.; Miyoshi, M.; Ikeda, I. *J. Am. Chem. Soc.* **1990**, *112*, 2813−2814. (b) Kurosawa, H.; Kajimaru, H.; Ogoshi, S.; Yoneda, H.; Miki, K.; Kasai, N.; Murai, S.; Ikeda, I. *J. Am. Chem. Soc.* **1992**, *114*, 8417−8424.

(8) Frisch, M. J.; Trucks, G. W.; Schlegel, H. B.; Scuseria, G. E.; Robb, M. A.; Cheeseman, J. R.; Scalmani, G.; Barone, V.; Mennucci, B.; Petersson, G. A.; Nakatsuji, H.; et al. *Gaussian09*, Revision D.01; Gaussian, Inc.: Wallingford, CT, 2013.

(9) Tao, J.; Perdew, J. P. *Phys. Rev. Lett.* **2003**, *91*, 146401−146404.

(10) (a) Schäfer, A.; Horn, H.; Ahlrichs, R. *J. Chem. Phys.* **1992**, *97*, 2571−2577. (b) Weigend, F.; Ahlrichs, R. *Phys. Chem. Chem. Phys.* **2005**, *7*, 3297−3305. (c) Weigend, F. *Phys. Chem. Chem. Phys.* **2006**, *8*, 1057−1065.

(11) (a) Grimme, S.; Antony, J.; Ehrlich, S.; Krieg, H. *J. Chem. Phys.* **2010**, *132*, 154104. (b) Grimme, S.; Ehrlich, S.; Goerigk, L. *J. Comput. Chem.* **2011**, *32*, 1456−1465.

(12) Andrae, D.; Haeusserman, U.; Dolg, M.; Stoll, H. *Theor. Chim. Acta* **1990**, *77*, 123−141.

(13) Weigend, F. *Phys. Chem. Chem. Phys.* **2006**, *8*, 1057−1065.

(14) Hratchian, H. P.; Schlegel, H. B. *J. Chem. Phys.* **2004**, *120*, 9918−9924.

(15) Grimme, S. *J. Chem. Phys.* **2006**, *124*, 034108.

(16) (a) Barone, V.; Cossi, M. *J. Phys. Chem. A* **1998**, *102*, 1995−2001. (b) Cossi, M.; Rega, N.; Scalmani, G.; Barone, V. *J. Comput. Chem.* **2003**, *24*, 669−681.

(17) (a) Reed, A. E.; Curtiss, L. A.; Weinhold, F. *Chem. Rev.* **1988**, *88*, 899−926. (b) Glendening, E. D.; Reed, A. E.; Carpenter, J. E.; Weinhold, F. *NBO*, version 3.1; University of Wisconsin: Madison, WI.

(18) (a) Bickelhaupt, F. M.; van Eikema Hommes, N. J. R.; Fonseca Guerra, C.; Baerends, E. J. *Organometallics* **1996**, *15*, 2923−2931. (b) Bickelhaupt, F. M.; Fonseca Guerra, C.; Handgraaf, J. W.; Baerends, E. J. *J. Comput. Chem.* **2004**, *25*, 189−210.

(19) te Velde, G.; Bickelhaupt, F. M.; Baerends, E. J.; Fonseca Guerra, C.; van Gisbergen, S. J. A.; Snijders, J. G.; Ziegler, T. *J. Comput. Chem.* **2001**, *22*, 931−967.

(20) (a) Clementi, E.; Roetti, C. *At. Data Nucl. Data Tables* **1974**, *14*, 177−478. (b) McLean, A. D.; Mclean, R. S. *At. Data Nucl. Data Tables* **1981**, *26*, 197−381. (c) Snijders, J. G.; Vernooijs, P.; Baerends, E. J. *At. Data Nucl. Data Tables* **1981**, *26*, 483−581. (d) Chong, D. P.; Lenthe, E. V.; Gisbergen, S. V.; Baerends, E. J. *J. Comput. Chem.* **2004**, *25*, 1030−1036.

(21) van Lenthe, E.; Baerends, E. J.; Snijders, J. G. *J. Chem. Phys.* **1994**, *101*, 9783−9792.

(22) (a) Morokuma, K. *J. Chem. Phys.* **1971**, *55*, 1236−1244. (b) Ziegler, T.; Rauk, A. *Inorg. Chem.* **1979**, *18*, 1755−1759. (c) Ziegler, T.; Rauk, A. *Inorg. Chem.* **1979**, *18*, 1558−1565.

(23) Fernández, I.; Bickelhaupt, F. *Chem. Soc. Rev.* **2014**, *43*, 4953−4967.

(24) (a) Luparia, M.; Oliveira, M. T.; Audisio, D.; Frébault, F.; Goddard, R.; Maulide, N. *Angew. Chem., Int. Ed.* **2011**, *50*, 12631−12635. (b) Audisio, D.; Luparia, M.; Teresa, O.; Klütt, M. N. *Angew. Chem., Int. Ed.* **2012**, *51*, 7314−7317. (c) Audisio, D.; Gopakumar, G.; Xie, L.-G.; Alves, L. G.; Wirtz, C.; Martins, A. M.; Thiel, W.; Farès, C.; Maulide, N. *Angew. Chem., Int. Ed.* **2013**, *52*, 6313−6316.

(25) (a) Knühl, G.; Sennhenn, P.; Helmchen, G. *J. Chem. Soc., Chem. Commun.* **1995**, 1845−1946. (b) Helmchen, G.; Ernst, M. *Angew. Chem.* **2002**, *41*, 4054−4056. (c) Seemann, M.; Schöller, M.; Kudis, S.; Helmchen, G. *Eur. J. Org. Chem.* **2003**, 2122−2127.

(26) Ahlquist, M.; Fristrup, P.; Tanner, D.; Norrby, O.-P. *Organometallics* **2006**, *252*, 2066−2073.

(27) Bühl, M.; Kabrede, H. *J. Chem. Theory Comput.* **2006**, *2*, 1282−1290.

(28) Steinmetz, M.; Grimme, S. *ChemistryOpen* **2013**, *2*, 115−124.

(29) (a) Karton, A.; Tarnopolsky, A.; Lamère, J.-F.; Schatz, G. C.; Martin, J. M. L. *J. Phys. Chem. A* **2008**, *112*, 12868−12886. (b) Grimme, S.; Goerigk, L. *J. Chem. Theory Comput.* **2011**, *7*, 291−309. (c) Jiang, W.; Laury, M. L.; Powell, M.; Wilson, A. K. *J. Chem. Theory Comput.* **2012**, *8*, 4102−4111. (d) Laury, M. L.; Wilson, A. K. *J. Chem. Theory Comput.* **2013**, *9*, 3939−3946. (e) Brémond, É.; Kalhor, M. P.; Bousquet, D.; Mignon, P.; Ciofini, I.; Adamo, C.; Cortona, O.; Chermette, H. *Theor. Chem. Acc.* **2013**, *132*, 1401−1413.

(30) The energies of all computed structures with both functionals are available in the Supporting Information.

(31) (a) Chandrasekhar, J.; Smith, S. F.; Jorgensen, W. L. *J. Am. Chem. Soc.* **1984**, *106*, 3049−3050. (b) Cossi, M. C.; Adamo, A.; Barone, B. *Chem. Phys. Lett.* **1998**, *297*, 1−7. (c) Mohamed, A.; Jensen, F. *J. Phys. Chem. A* **2001**, *105*, 3259−3268.

(32) There is an interesting preference for the ligand to be positioned *cis* to the dissociating chloride in **TS-A$_{L1}$** structures, which is enhanced with electron-donating groups but is not present in the extreme electron-deficient case (**MA**). This preference originates from orbital interactions between the HOMO of the palladium fragment and the

σ^* orbital of the cleaving C−Cl bond, which become stronger with electron-donating groups.
(33) The Pd···Cl association in the *anti* pathway is confirmed by inspection of the IRC diagram.
(34) Carrion, F.; Dewar, M. J. S. *J. Am. Chem. Soc.* **1984**, *106*, 3531−3539.
(35) Ess, D. H.; Wheeler, S. E.; Iafe, R. G.; Xu, L.; Çelebi-Ölçüm, N.; Houk, K. N. *Angew. Chem., Int. Ed.* **2008**, *47*, 7592−7601.
(36) (a) Çelebi-Ölçüm, N.; Ess, D. H.; Aviyentie, V.; Houk, K. N. *J. Am. Chem. Soc.* **2007**, *129*, 4528−4529. (b) Çelebi-Ölçüm, N.; Ess, D. H.; Aviyente, V.; Houk, K. N. *J. Org. Chem.* **2008**, *73*, 7472−7480.
(37) Full tables of energies from the EDA for all reactant complexes and transition states are available in the Supporting Information.
(38) A similar analysis in which the reaction coordinate is projected along the C−Cl bond distance has been performed and is available in the Supporting Information.
(39) (a) Corey, E. J.; Boaz, N. W. *Tetrahedron Lett.* **1984**, *25*, 3063−3066. (b) Starý, I.; Zajíček, J.; Kočovsky, P. *Tetrahedron Lett.* **1992**, *48*, 7229−7250.
(40) Distortion profiles of the NBO charge transfer illustrate this point (see the Supporting Information).
(41) Mitoraj, M.; Michalak, A. *J. Mol. Model.* **2007**, *13*, 347−355.
(42) A corresponding NOCV analysis is available in the Supporting Information.
(43) Electron density parameters from an AIM analysis are also suggestive of a stronger Pd−Cl interaction along the reaction coordinate for complexes with electron-deficient ligands (see the Supporting Information).